ELSEVIER

Journal of Fluids and Structures 24 (2008) 589–603

JOURNAL OF FLUIDS AND STRUCTURES

www.elsevier.com/locate/jfs

Experimental investigation of coaxial side branch resonators

P. Oshkai*, T. Yan

Department of Mechanical Engineering, University of Victoria, P.O. Box 3055, STN CSC, Vic., BC, Canada V8W 3P6

Received 10 August 2007; accepted 25 October 2007
Available online 20 February 2008

Abstract

Digital particle image velocimetry is employed to investigate acoustically-coupled flow past a coaxial deep cavity (side branch) resonator mounted in a duct. The emphasis is on the effect of the separation between the coaxial side branches on the interaction between separated shear layers that form across the side branch openings. Various resonator geometries are characterized in terms of patterns of instantaneous and time-averaged flow velocity, vorticity, and streamline topology at several phases of the acoustic cycle. In addition, phase-averaged images of the flow in conjunction with unsteady pressure measurements are evaluated in order to provide insight into the mechanisms of acoustic power generation. Generally speaking, the acoustic source undergoes a significant transformation as the distance between the coaxial side branches changes. As the distance between the side branches decreases, interaction between the associated oscillating shear layers results in substantial changes in the spatial structure of the acoustic source region.

Keywords: Flow-acoustic coupling; Side branch resonators; PIV

1. Introduction

When a turbulent flow passes over a deep cavity (side branch) mounted in a duct, a shear layer is created between the moving fluid in the main duct and the stationary fluid in the side branch. Flow-acoustic coupling occurs when the frequency of the hydrodynamic mode of the shear layer oscillation matches the resonant acoustic mode of the side branch. The resonant acoustic waves interact with small-scale vortical structures in the shear layer. This interaction results in formation of large-scale vortices that are convected downstream and eventually release part of their energy to the acoustic field. This energy contributes to the increase of the amplitude of the acoustic waves and, in turn, to the radiated noise.

Over the years, flow-acoustic coupling in cavities has been a subject of numerous investigations. Detailed reviews of noise and vibration generation in cavities can be found, for example in Rockwell and Naudascher (1978). Bruggeman et al. (1989, 1991), Nelson et al. (1981), Ziada and Bühlmann (1992), and Kriesels et al. (1995) specifically addressed deep cavity resonators using experimental and theoretical approaches. In addition, Nelson et al. (1983), Bruggeman et al. (1991) and Kriesels et al. (1995) employed various numerical vortex models in conjunction with the theoretical concepts developed by Howe (1975) to study the mechanisms of acoustic power generation. Radavich et al. (1999)

*Corresponding author. Tel.: +1 250 721 8922; fax: +1 250 721 6051.
E-mail address: poshkai@me.uvic.ca (P. Oshkai).

0889-9746/$ - see front matter © 2007 Elsevier Ltd. All rights reserved.
doi:10.1016/j.jfluidstructs.2007.10.008

employed computational fluid dynamics to simulate the flow-acoustic coupling and determine the location and timing of the acoustic power production during an acoustic oscillation cycle.

Specifically related to the present study are the experimental investigations of Ziada (1994) and Oshkai et al. (2005), who studied formation and propagation of vortices during an acoustic cycle using qualitative and quantitative flow visualization methods, respectively. In addition, Dequand et al. (2003a, b) studied behaviour of acoustically-coupled flows over a Helmholtz resonator. The authors identified characteristic flow regimes and provided numerical and analytical models of the flow. More recently, Oshkai et al. (2005) employed digital particle image velocimetry (DPIV) to characterize the effect of separation of coaxial side branches in terms of instantaneous and time-averaged flow patterns. The present study focuses on a coaxial side branch system, which involves two side branches mounted on the opposite sides of a rectangular duct and inline with each other. The objective is to investigate the effect of the side branch separation on the structure of the acoustic power source by applying a phase-averaging process to the global quantitative images of the flow corresponding to various values of the main duct width.

2. Experimental system and techniques

2.1. Coaxial side branch resonator

The experiments were performed using air as the working fluid. A flow facility, which consists of a plenum chamber, a main duct, and a coaxial side branch arrangement, allows variations of the channel geometry, optical access to the separated flow area(s), as well as ability to perform acoustic pressure measurements. The schematic of the coaxial side branch resonator mounted in the main duct is provided in Fig. 1.

The main duct of rectangular cross-section was made of plexiglas. The duct had a streamwise length of 492 mm and a height (the out-of-page dimension) of 25.4 mm. Two coaxial side branches were mounted on the opposite sides of the main duct, 454 mm downstream of the duct inlet. The side branches had a square cross-section, and were constructed of a 3.2-mm-thick aluminium. The main duct extended for additional 12.6 mm downstream of the side branch arrangement.

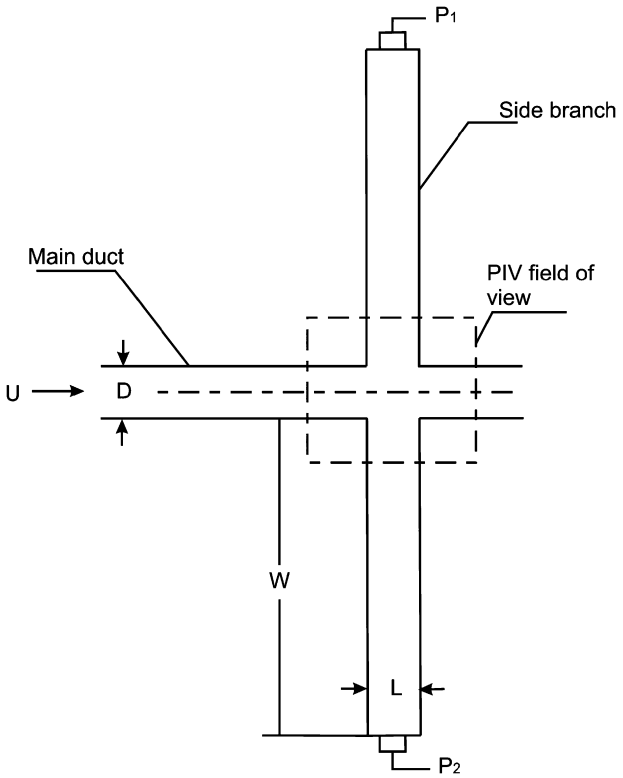

Fig. 1. Schematic of the coaxial side branch resonator.

In the present investigation, the flow features are compared for the two cases corresponding to a relatively large value of the main duct width ($D = 13$ mm) and a smaller value of $D = 6.5$ mm. Dimensions of the individual side branches ($L = 25.4$ mm, $W = 483$ mm) were chosen to provide an opportunity for observation of at least two distinct hydrodynamic modes of the shear layer oscillation for both values of the main duct width.

2.2. Pressure measurements

Measurements of unsteady pressure were performed using piezoelectric microphone pressure transducers, indicated as P_1 and P_2 in Fig. 1. The pressure transducers had a nominal sensitivity of 1500 mV/psi and were deployed at the dead ends of side branch resonator. The pressure signals were converted to a digital form at the time of acquisition.

The experimental results of Kriesels et al. (1995) and Ziada (1994) provided a basis for the selection of a locked-on flow tone. The data presented herein correspond to two acoustic resonant frequencies. The investigations are focused on the dominant frequency of acoustic oscillations of $f = 545$ Hz that are excited by the first hydrodynamic oscillation mode and the acoustic frequency $f = 840$ Hz that are excited by the second shear layer oscillation mode. The pressure signals were acquired at the frequency of 8192 samples/s. The time trace of the pressure signal P_1 was employed as a phase reference for the image acquisition.

2.3. Techniques of particle image velocimetry

Quantitative flow visualization was accomplished by employing a technique of DPIV. The air flow was seeded with tracers with the typical diameter of approximately 1 μm. The amount of seeding particles that were introduced into the flow stream was optimized in order to ensure negligible effect on the speed of sound and acoustic damping while providing sufficient density for the flow visualization purposes. Images of the particles, which were illuminated by a laser, were captured by a high-resolution digital camera. These images were then processed on a computer to yield the global instantaneous flow velocity measurements, distributions of the out-of-plane vorticity, as well as phase- and time-averaged flow parameters. The displacement of the particles was recorded as a pair of images, each exposed once. The recorded particle displacement field was measured locally across the whole field of view of the images, scaled by the image magnification and then divided by the known laser pulse separation to obtain flow velocity at each point. The CCD camera was positioned as shown in Fig. 2. Depending on the flow velocity and the factor of magnification of the camera lens, the delay of the two pulses was chosen such that adequate displacements of the particle images on the CCD are obtained.

For the present study, a lens with a focal length of 60 mm was used in conjunction with a 1376×1040 pixel CCD to provide a physical resolution of the velocity vector field of 0.22×0.22 mm. The system provided 4.9 cross-correlated images per second.

The trigger signal to the laser was recorded together with the acoustic pressure signals. This provided the information regarding the phase of acquisition of each velocity field with respect to a typical acoustic cycle.

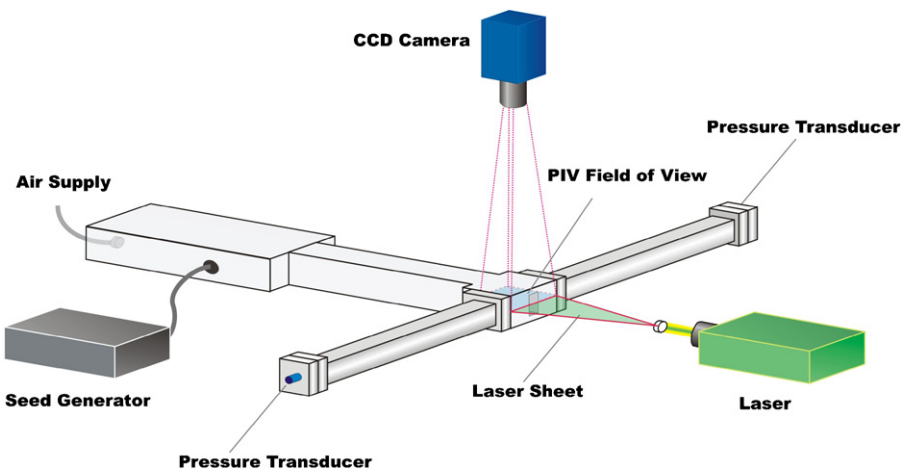

Fig. 2. Schematic of the PIV set-up.

2.4. Time- and phase-averaging of PIV images

A total of 2000 images were acquired and used in the calculation of the time-averaged flow parameters. In addition, a phase-locking technique was employed to acquire images of the flow throughout a typical acoustic cycle. The camera was controlled to take 200 cross-correlated pairs of images at each phase of the cycle using a real-time acoustic pressure signal as a reference. Ensemble-averaging of the PIV images acquired at the same phase was performed to produce a single global quantitative representation of the flow at each phase.

Phase φ of the image acquisition was defined as the phase difference between the occurrence of zero crossing of pressure signal from a negative to a positive value and the image acquisition time. The acoustic pressure signal was essentially sinusoidal, and the dominant frequency was well-separated from other components. Therefore, the acoustic pressure signal was not filtered, and the ambiguity of the phase calculation was estimated based on the predominant frequency of the shear layer oscillation mode (545 Hz) and the data acquisition frequency. The period of the data acquisition (0.00002 s) corresponds to approximately 4° of the complete oscillation period, which results in the ambiguity of $\pm 4°$ in the phase calculation.

3. Effect of the main duct width

3.1. Instantaneous flow patterns

Instantaneous images of flow velocity $\boldsymbol{V}$ and out-of-plane vorticity ω_z for wide duct ($D = 13$ mm) at the first hydrodynamic oscillation mode are shown in Fig. 3. The images correspond to a phase in the acoustic oscillation cycle, which is indicated by a circle in the inset schematic. The mean flow velocity is $U = 38$ m/s and the acoustic frequency is $f = 545$ Hz, which yields a Strouhal number of $\mathrm{Sr} = fL/U = 0.36$. The observed value of the dimensionless acoustic velocity U_{ac}/U for this case is equal to 0.0005. The acoustic velocity amplitude U_{ac} is determined from the acoustic pressure amplitude P: $U_{ac} = P/\rho_0 c_0$, where ρ_0 is the mean fluid density and c_0 is the speed of sound.

Instantaneous patterns of velocity and vorticity show that unsteady vortical structures of multiple scales are present in the top and bottom shear layers. The small-scale Kelvin–Helmholtz vortices that initially form in the separated shear layers in the vicinity of the upstream corners of the side branch resonator eventually roll up into larger-scale structures as they are convected downstream along the mouth of the side branch. These large-scale vortices generally have lower peak vorticity than the original Kelvin–Helmholtz vortices, but possess greater energy due to larger circulation values and increased convective speed. Images presented herein correspond to the first hydrodynamic mode of the shear layer oscillation, when one large-scale vortex forms in the shear layer during a typical oscillation cycle.

When the main duct is relatively wide, as shown in Fig. 3, the two shear layers that form across the top and bottom side branches impinge upon the downstream corners of the corresponding side branches. In this case, the structure of

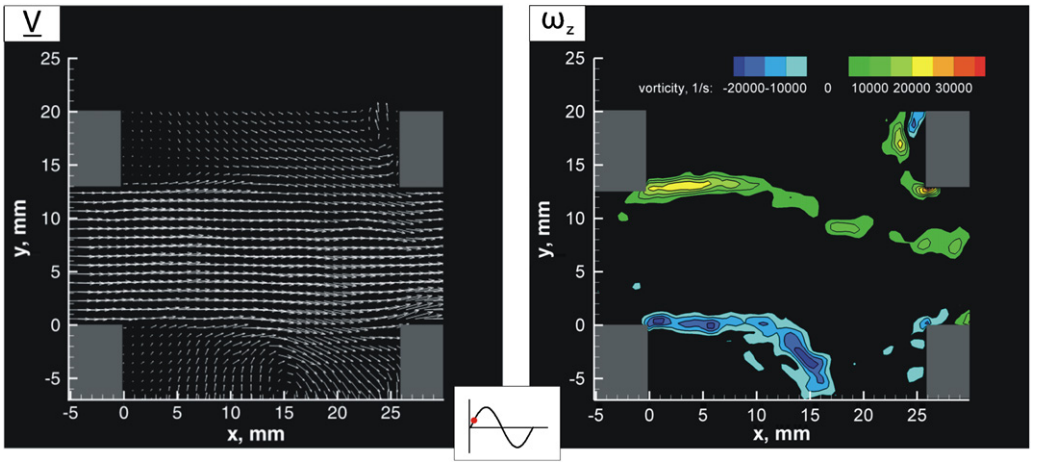

Fig. 3. Patterns of instantaneous velocity vector (left) and vorticity (right) corresponding to the first hydrodynamic oscillation mode for the case of a wide main duct ($D = 13$ mm). The minimum positive and negative contour levels are $\omega^{+}_{\min} = 5000\,\mathrm{s}^{-1}$ and $\omega^{-}_{\min} = -5000\,\mathrm{s}^{-1}$, respectively. The contour increment is $\Delta\omega = 5000\,\mathrm{s}^{-1}$.

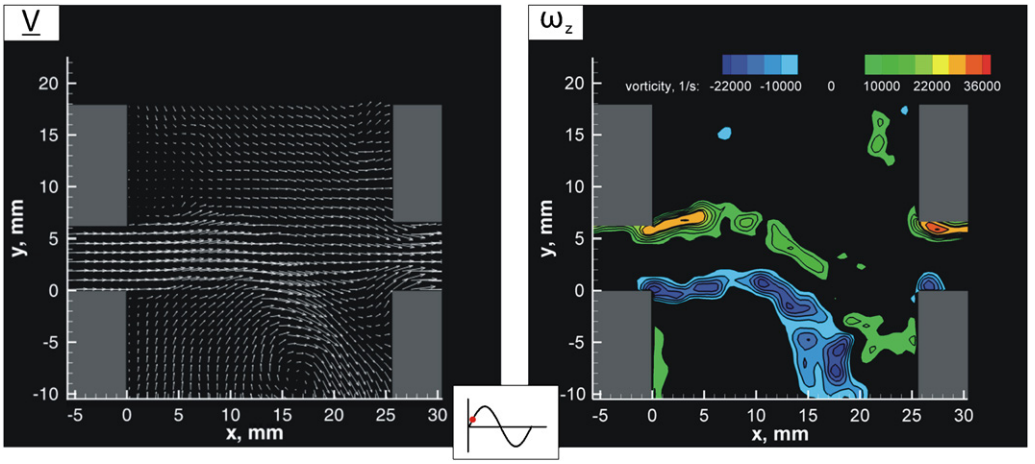

Fig. 4. Patterns of instantaneous velocity vector (left) and vorticity (right) corresponding to the first hydrodynamic oscillation mode for the case of a narrow main duct ($D = 6.5$ mm). The minimum positive and negative contour levels are $\omega^{+}_{\min} = 6000\,\mathrm{s}^{-1}$ and $\omega^{-}_{\min} = -6000\,\mathrm{s}^{-1}$, respectively. The contour increment is $\Delta\omega = 4000\,\mathrm{s}^{-1}$.

the acoustic source of the coaxial side branch resonator is characterized by regions of elevated values of the generated acoustic power that correspond to development of large-scale vortical structures in the shear layers.

This situation is in marked contrast to the shear layer interaction that occurs at the lower value of the main duct width ($D = 6.5$ mm) shown in Fig. 4. When the main duct width is sufficiently low, the bottom shear layer can interact with the top shear layer. This flow behaviour suggests that the structure of the acoustic power source will change significantly as the main duct width is decreased.

3.2. Phase-averaged flow patterns

3.2.1. Phase-averaged flow patterns at the first hydrodynamic oscillation mode

Fig. 5 shows the phase-averaged flow patterns corresponding to the first hydrodynamic mode for the two values of the main duct width D at the phase of the acoustic cycle $\varphi = 10^{\circ}$. The left and right columns of images in Fig. 5 correspond to the values of D of 13 and 6.5 mm, respectively. The images show plots of phase-averaged flow velocity $\langle \boldsymbol{V} \rangle_p$, vorticity $\langle \omega_z \rangle_p$, and streamline patterns (from top to bottom). At this phase, the acoustic velocity is directed into the upper side branch, and a new vortex is formed at the upstream edge of upper side branch (indicated in the vorticity plot). The vortex in the lower shear layer has been fully developed and convected downstream. The patterns of the streamline topology correspond to the reference frame moving from left to right with the speed of $0.5U$, which approximates the average convective speed of the large-scale vortices in the shear layers. The plots show higher levels of circulation of the large-scale vortices in the case of the narrower main duct. In addition, the interaction between the vortical structures in the top and the bottom shear layers is increased as the main duct becomes narrower.

When the acoustic velocity changes sign, a new vortex starts to develop at the upstream edge of either the upper or the lower side branch. This vortex is then convected downstream, and its circulation is increased. At the later phase ($\varphi = 240^{\circ}$), shown in Fig. 6, the positive vortex in the upper shear layer impinges on the downstream corner of the side branch. At the same time, a new negative vortex develops in the lower shear layer.

3.2.2. Phase-averaged flow patterns at the second hydrodynamic oscillation mode

The figures shown in this section correspond to the second hydrodynamic mode of the shear layer oscillation, where the side branch resonators are excited at the fifth acoustic mode ($f = 840$ Hz). In the case of the wide main duct, the mean flow velocity is 26 m/s, which corresponds to the Strouhal number $\mathrm{Sr} = fL/U = 0.82$. The maximum dimensionless value of the one-dimensional acoustic velocity U_{ac}/U for this case is 0.00017. In contrast to the first hydrodynamic mode, where only one large-scale vortex is observed in the upper or lower shear layer, two vortices are formed in each shear layer during a typical oscillation cycle. At the phase $\varphi = 10^{\circ}$ (shown in Fig. 7), the acoustic velocity is directed into the upper side branch. The vorticity plots in the second row show that the two vortices in the upper shear layer are pulled inside the branch by the acoustic flux. Meanwhile, the lower vortices are pushed out of the

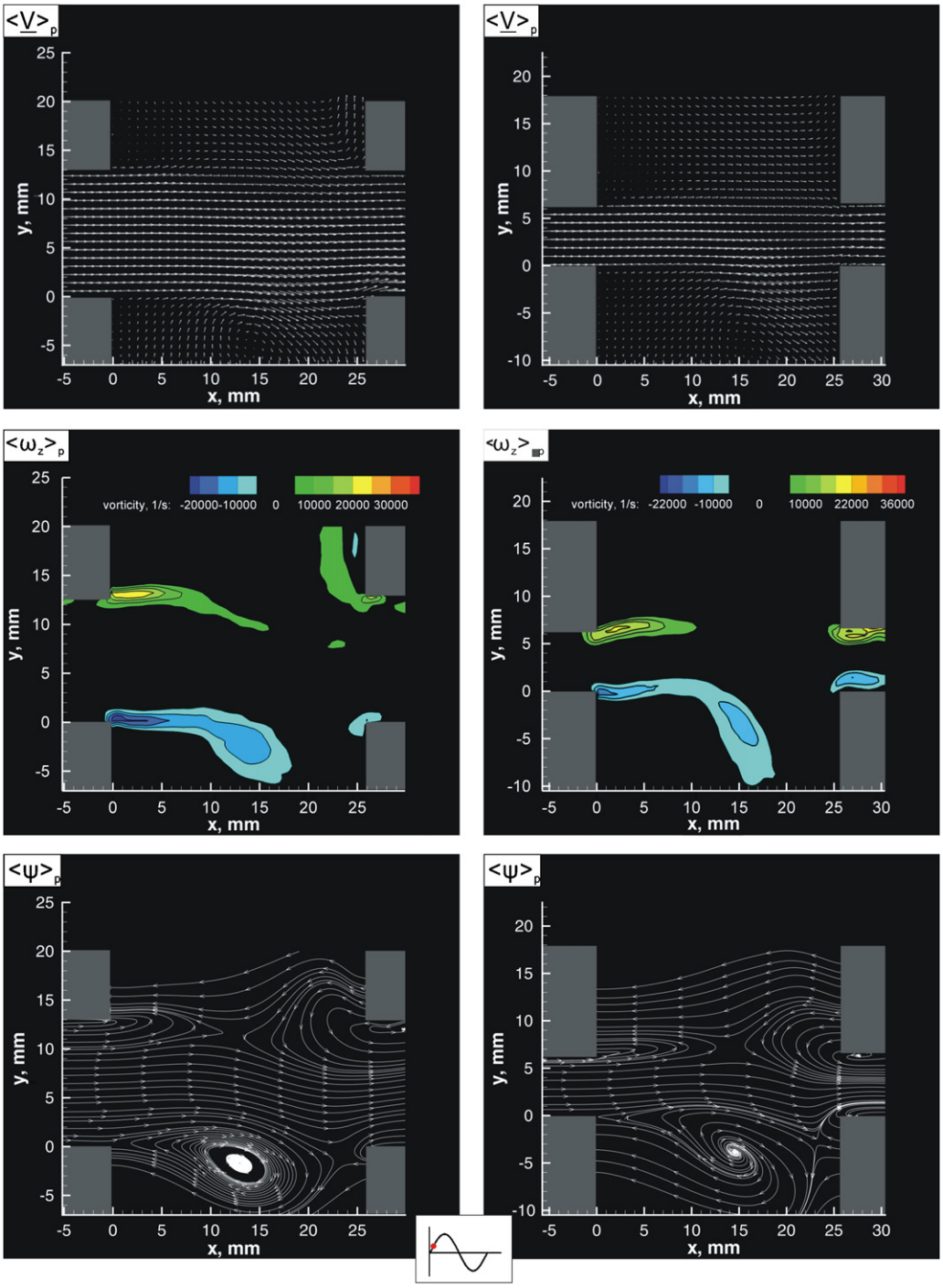

Fig. 5. Phase-averaged streamwise flow patterns corresponding to the first hydrodynamic oscillation mode at $\varphi = 10$. The minimum positive and negative contour levels for the case of $D = 13\,\text{mm}$ (left column) are $\langle\omega\rangle^{+}_{p_{\min}} = 5000\,\text{s}^{-1}$ and $\langle\omega\rangle^{-}_{p_{\min}} = -5000\,\text{s}^{-1}$, respectively. The contour increment is $\Delta\langle\omega\rangle_p = 5000\,\text{s}^{-1}$. The corresponding values for the case of $D = 6.5\,\text{mm}$ (right column) are $\langle\omega\rangle^{+}_{p_{\min}} = 6000\,\text{s}^{-1}$, $\langle\omega\rangle^{-}_{p_{\min}} = -6000\,\text{s}^{-1}$, and $\Delta\langle\omega\rangle_p = 4000\,\text{s}^{-1}$.

lower side branch. In the upper shear layer, the first vortex that is located near the upstream corner of the side branch is in the stage of development. The second vortex that has been formed completely is convecting along with the mean flow towards the trailing edge of the upper side branch. In the case of the narrow duct, the pressure amplitude is 0.0006 psi,

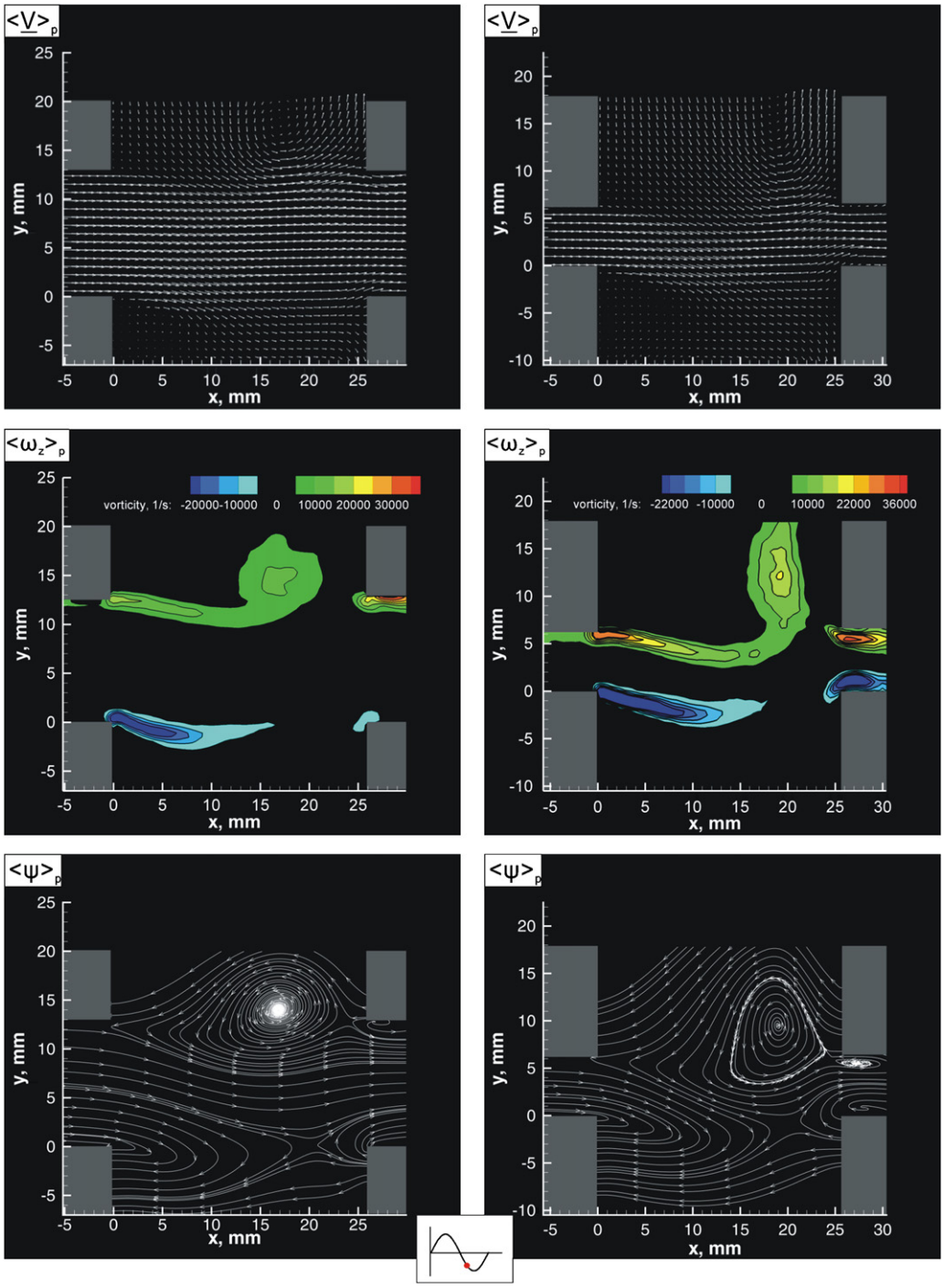

Fig. 6. Phase-averaged streamwise flow patterns corresponding to the first hydrodynamic oscillation mode at $\varphi = 240^{\circ}$. The minimum positive and negative contour levels for the case of $D = 13\,\text{mm}$ (left column) are $\langle\omega\rangle^{+}_{p_{\min}} = 5000\,\text{s}^{-1}$ and $\langle\omega\rangle^{-}_{p_{\min}} = -5000\,\text{s}^{-1}$, respectively. The contour increment is $\Delta\langle\omega\rangle_p = 5000\,\text{s}^{-1}$. The corresponding values for the case of $D = 6.5\,\text{mm}$ (right column) are $\langle\omega\rangle^{+}_{p_{\min}} = 6000\,\text{s}^{-1}$, $\langle\omega\rangle^{-}_{p_{\min}} = -6000\,\text{s}^{-1}$, and $\Delta\langle\omega\rangle_p = 4000\,\text{s}^{-1}$.

which corresponds to the dimensionless value of the acoustic velocity $U_{ac}/U = 0.00036$. In comparison with the case of the wide main duct, the acoustic pressure is significantly increased, which suggests that the interaction between the shear layers results in more energy being released from the vortical structures. The peak value of absolute vorticity is

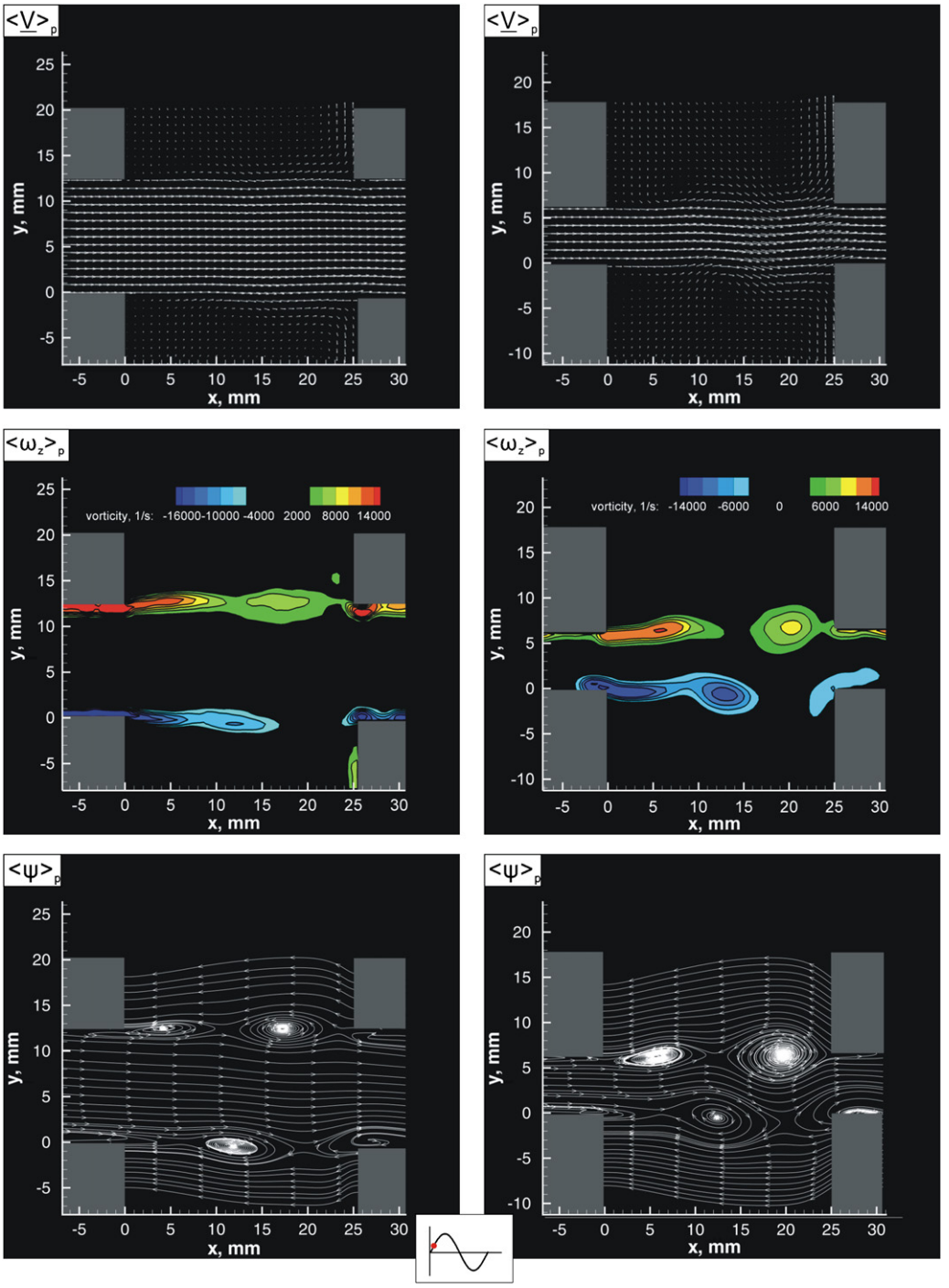

Fig. 7. Phase-averaged streamwise flow patterns corresponding to the second hydrodynamic oscillation mode at $\varphi = 10^{\circ}$. The minimum positive and negative contour levels for the case of $D = 13$ mm (left column) are $\langle\omega\rangle^{+}_{p_{\min}} = 4000\,\mathrm{s}^{-1}$ and $\langle\omega\rangle^{-}_{p_{\min}} = -6000\,\mathrm{s}^{-1}$, respectively. The contour increment is $\Delta\langle\omega\rangle_p = 2000\,\mathrm{s}^{-1}$. The corresponding values for the case of $D = 6.5$ mm (right column) are $\langle\omega\rangle^{+}_{p_{\min}} = 4000\,\mathrm{s}^{-1}$, $\langle\omega\rangle^{-}_{p_{\min}} = -4000\,\mathrm{s}^{-1}$, and $\Delta\langle\omega\rangle_p = 2000\,\mathrm{s}^{-1}$.

$14\,000\,\mathrm{s}^{-1}$, which is observed near the upstream edges of both side branches. The vorticity plot indicates that the circulation values are larger than those observed in the case of the wide duct. Two well-defined vortices are apparently present over the cavity openings in this case. Since the acoustic pressures inside the coaxial side branches are

180° out-of-phase, the vortices in the lower shear layer lead the vortices in the upper shear layer in time by one-half of an acoustic period. The large-scale vortex in the lower shear layer is located approximately 12 mm downstream of the leading edge. The distance between the centres of vortices in the upper and lower shear layers is approximately 7 mm. The streamline patterns indicate that the interaction between the upper and the lower shear layers in the vicinity of the separation region is less pronounced compared to the first shear layer oscillation mode.

During the first half of acoustic period, the small-scale vorticity concentrations roll up into the large-scale vortex. The previously-formed large-scale vortex starts to interact with the downstream edge. The convective speed of the vortices is such that the vortex traverses approximately a quarter of the side branch length during one half of the acoustic period. As the acoustic phase increases, the acoustic velocity reverses its direction and points out of the upper side branch. The vortices in the upper shear layer are forced downward and a new vortex develops at the upstream edge of the lower side branch.

4. Acoustic power

4.1. Acoustic power calculation

The pressure fluctuations across the flow region, which are induced by unsteady vortex shedding from the upstream edges of the side branches are coupled with the acoustic waves in the resonator. When the shear layer frequency matches the natural frequency of the resonator, the acoustic waves inside the coaxial side branches are amplified. Therefore, the shear layers that form across the mouths of the side branches are considered to be the source of the generated acoustic power.

The acoustic energy produced by the vortex shedding can accumulate due to the presence of the acoustic resonating modes with a high quality factor. The instantaneous acoustic power P_{ac} generated by vorticity ω, within a volume V can be obtained from

$$P_{ac} = -\iiint_V \rho_0(\boldsymbol{\omega} \times \boldsymbol{V}) \cdot \boldsymbol{u}_{ac}\, \mathrm{d}V, \tag{1}$$

where ρ_0 is the fluid density, $\boldsymbol{V}$ is the fluid velocity, and $\boldsymbol{u}_{ac}$ is the acoustic particle velocity (Howe, 1975).

Eq. (1), which is based on the vortex sound theory, provides a general approximation for the calculation of the acoustic power. It should be noted that recent studies suggest that the flow-acoustic coupling for the cases of the narrow main duct are more accurately described by a jet-drive model (Dequand, 2003b).

Assuming that the side branches act as quarter-wavelength resonators and neglecting the effects of friction and wall vibration, the acoustic velocity $\boldsymbol{u}_{ac}$ in the cross-junction is modelled numerically by placing a source–sink pair of variable strength m at the ends of the side branches:

$$u_{ac} = m\left(\frac{1}{y-a} - \frac{1}{y+a}\right), \tag{2}$$

where a is the side branch depth measured from the centerline of the channel, as shown in Fig. 8. The source strength m is

$$m = U_{ac} \sin(2\pi f t), \tag{3}$$

where f is the frequency of the acoustic pressure signal measured at the end of a closed side branch. The acoustic velocity amplitude U_{ac} can be determined from the acoustic pressure amplitude P: $U_{ac} = P/\rho_0 c_0$, where ρ_0 is the mean fluid density and c_0 is the speed of sound.

Regarding the uncertainty of the acoustic power results, there are several sources of error in acoustic power calculation, including the uncertainty in determination of the phase of the acoustic cycle, velocity and vorticity values. Due to the approximate nature of the acoustic power model and the simplified treatment of the acoustic velocity field, the error in the phase determination ($\pm 4°$) is expected to be dominant.

4.2. Phase-averaged acoustic power

4.2.1. Phase-averaged acoustic power at the first hydrodynamic oscillation mode

Fig. 9 shows patterns of generated acoustic power corresponding to the first hydrodynamic mode for the wide ($D = 13$ mm) and the narrow main duct ($D = 6.5$ mm) in the left and right columns, respectively. The three rows of images correspond to three successive phases of the acoustic oscillation cycle indicated by the location of the circle in

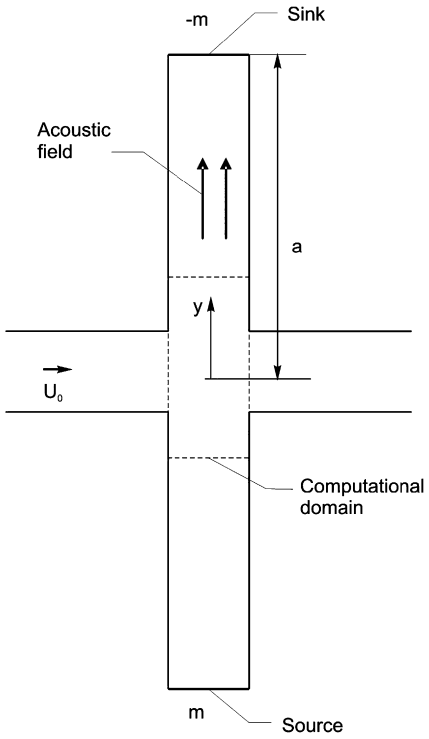

Fig. 8. Definition of parameters for acoustic power calculation.

the inset schematics in the middle of each row. The calculation of the acoustic power is based on the measured phase-averaged values of flow velocity and vorticity.

The first phase ($\varphi = 10^\circ$) corresponds to an instant when a new vortex starts to form at the upstream edge of upper side branch. The vortex absorbs energy from the acoustic field, resulting in the negative contribution to the acoustic power production, as indicated in the top row of images in Fig. 9. At the same time, the well-developed vortical structure in the lower shear layer is convected downstream. The energy is transferred from the vortex to the acoustic field, which is indicated by the positive contours of the generated acoustic power across the mouth of the lower side branch.

The middle row of images corresponds to the phase $\varphi = 170^\circ$. Vortical structures in both the upper and the lower shear layers develop further, and the peak values of the generated acoustic power in the flow field increase. It should be noted that the vortices in the upper shear layer continue to absorb the energy from the acoustic field, since the acoustic velocity u_{ac} is still positive at this instant, i.e. it is directed into the upper side branch.

The bottom row of images corresponds to the phase $\varphi = 240^\circ$. At this phase, the acoustic velocity is directed into the lower side branch, and the vorticity in the upper shear layer makes a positive contribution to the generated acoustic power.

For all three phases, the case of the narrow main duct ($D = 6.5$ mm) exhibits higher level of interaction between the upper and the lower shear layers, compared to the case of the wide duct ($D = 13$ mm). As a result, the vortices within the shear layers attain higher levels of circulation, which in turn results in the increased peak values of generated acoustic power.

The acoustic power contribution of the upper shear layer as a function of time during a typical acoustic oscillation cycle is shown in Fig. 10 for the case of the wide main duct ($D = 13$ mm). The first half of the period corresponds to the formation of large-scale vortical structures in the shear layers, while during the second half of the period, the vortices impinge on the downstream edge, and their energy is transferred to the acoustic field.

4.2.2. Phase-averaged acoustic power at the second hydrodynamic oscillation mode

For the second hydrodynamic oscillation mode, patterns of the phase-averaged acoustic power at three phases for the wide ($D = 13$ mm) and narrow main duct ($D = 6.5$ mm) are shown in Fig. 11. These three phases correspond to

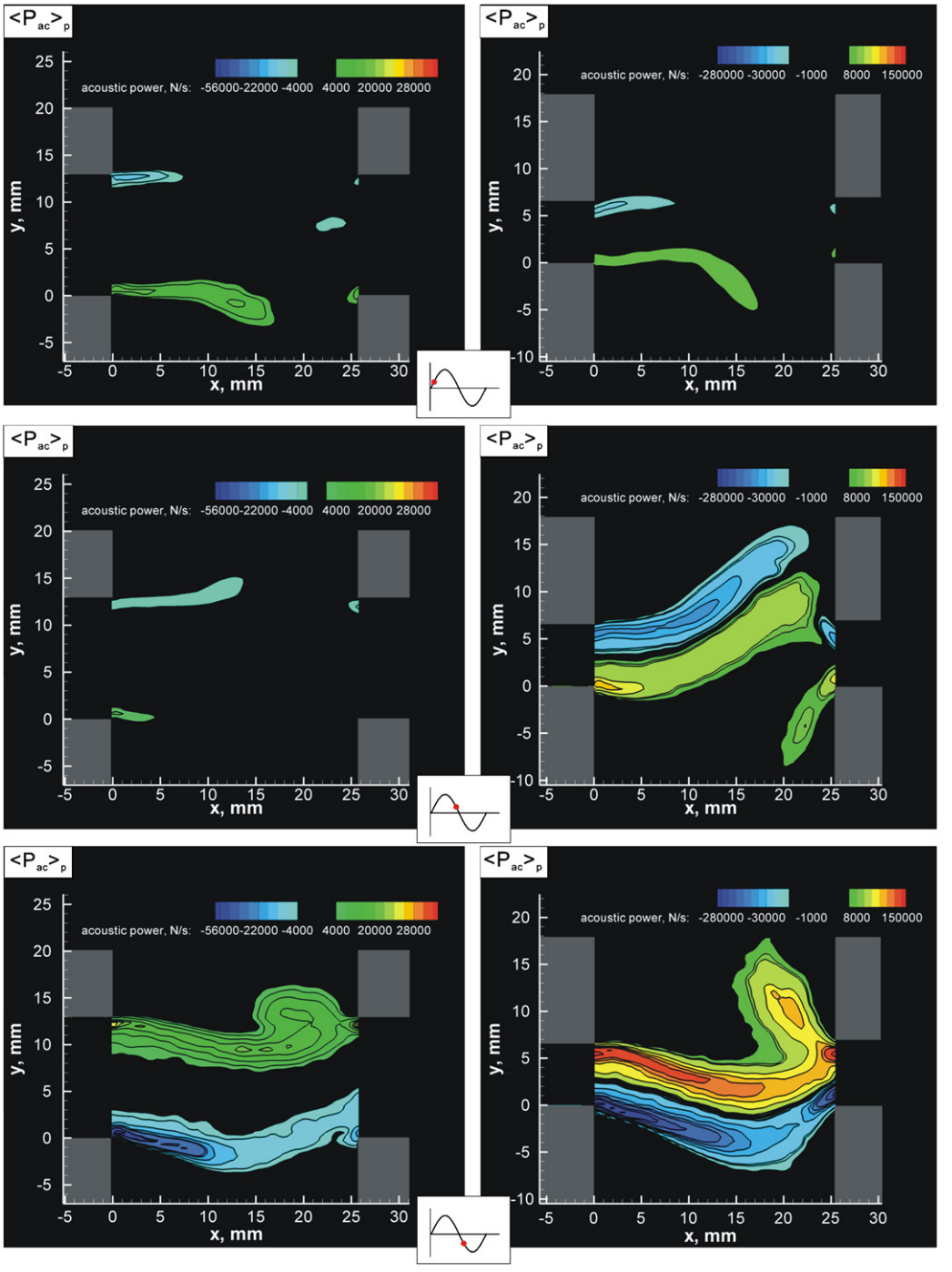

Fig. 9. Phase-averaged acoustic power corresponding to the first hydrodynamic oscillation mode. The top images illustrate the generated acoustic power at $\varphi = 10^{\circ}$. The minimum positive and negative contour levels for the case of $D = 13\,\text{mm}$ (left column) are $\langle\omega\rangle^{+}_{p_{\min}} = 4000\,\text{s}^{-1}$ and $\langle\omega\rangle^{-}_{p_{\min}} = -4000\,\text{s}^{-1}$, respectively. The contour increment is $\Delta\langle\omega\rangle_p = 6000\,\text{s}^{-1}$. The corresponding values for the case of $D = 6.5\,\text{mm}$ (right column) are $\langle\omega\rangle^{+}_{p_{\min}} = 4000\,\text{s}^{-1}$, $\langle\omega\rangle^{-}_{p_{\min}} = -4000\,\text{s}^{-1}$, and $\Delta\langle\omega\rangle_p = 20\,000\,\text{s}^{-1}$. In the middle images ($\varphi = 170^{\circ}$), for the case of $D = 13\,\text{mm}$ (left column), $\langle\omega\rangle^{+}_{p_{\min}} = 2000\,\text{s}^{-1}$, $\langle\omega\rangle^{-}_{p_{\min}} = -2000\,\text{s}^{-1}$, and $\Delta\langle\omega\rangle_p = 6000\,\text{s}^{-1}$. The corresponding values for the case of $D = 6.5\,\text{mm}$ (right column) are $\langle\omega\rangle^{+}_{p_{\min}} = 4000\,\text{s}^{-1}$, $\langle\omega\rangle^{-}_{p_{\min}} = -4000\,\text{s}^{-1}$, and $\Delta\langle\omega\rangle_p = 20\,000\,\text{s}^{-1}$. In the bottom images ($\varphi = 240^{\circ}$), for the case of $D = 13\,\text{mm}$ (left column), $\langle\omega\rangle^{+}_{p_{\min}} = 4000\,\text{s}^{-1}$, $\langle\omega\rangle^{-}_{p_{\min}} = -4000\,\text{s}^{-1}$, and $\Delta\langle\omega\rangle_p = 6000\,\text{s}^{-1}$. The corresponding values for the case of $D = 6.5\,\text{mm}$ (right column) are $\langle\omega\rangle^{+}_{p_{\min}} = 4000\,\text{s}^{-1}$, $\langle\omega\rangle^{-}_{p_{\min}} = -4000\,\text{s}^{-1}$, and $\Delta\langle\omega\rangle_p = 20\,000\,\text{s}^{-1}$.

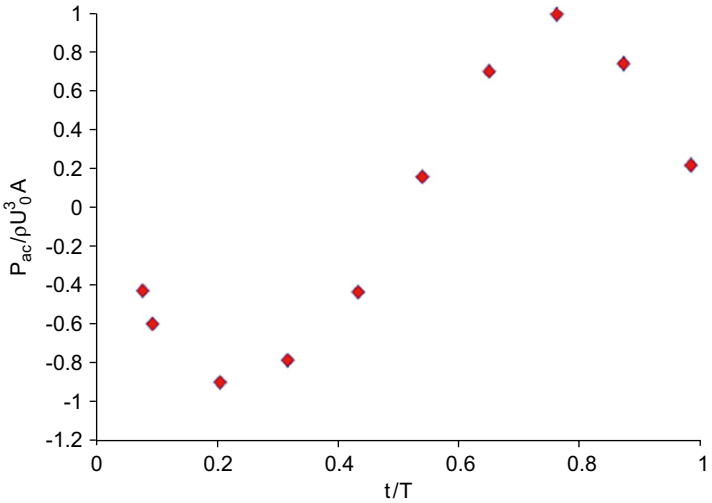

Fig. 10. Acoustic power generated by the upper shear layer during one period of acoustic oscillation.

$\varphi = 10^\circ$, 170°, and 240°. In the case of the wide main duct, at phase $\varphi = 10^\circ$, the source region with the peak amplitude of approximately 320 N/s spans over the mouth of the lower side branch. The highest power source region is located near the upstream corner of the junction between the main duct and the lower side branch. The weaker sink region dominates the larger area of the upper side branch opening. The acoustic velocity at this phase is directed into the upper side branch. The sign of the triple product $(\boldsymbol{\omega} \times \boldsymbol{v}) \cdot \boldsymbol{u}_{ac}$ corresponding to the top shear layer is negative, which means that the vorticies act as acoustic sinks. In the lower region of junction, the opposite sign of triple product results in the positive contribution of the lower shear layer.

At the phase of $\varphi = 170^\circ$, the power levels become significantly higher as a result of developed large-scale vortices that exhibit higher circulation levels. Since the acoustic velocity field did not change direction compared to the previous phase ($\varphi = 10^\circ$), the upper and lower shear layers still correspond to negative and positive contributions to acoustic power, respectively

At the phase $\varphi = 240^\circ$, the acoustic velocity is directed into the lower side branch. The triple product changes sign, which leads to the positive contribution from the upper shear layer and to formation of a sink region at the lower side. The elevated levels of the generated acoustic power occur over a large area in the flow field and the peak values are increased.

4.3. Time-averaged acoustic power

4.3.1. Time-averaged acoustic power at the first hydrodynamic oscillation mode

Patterns of the time-averaged acoustic power corresponding to the first shear layer oscillation mode are shown in Fig. 12. The left and right plots correspond to the wide and the narrow main ducts, respectively.

In the case of the wide duct ($D = 13$ mm), the upper and the lower shear layers develop, essentially, independently of each other. As a result, the structure of the acoustic power producing region exhibits two distinct source–sink pairs. The sinks correspond to the regions where the acoustic energy is absorbed by the flow field. These areas are indicated by the negative contours. The sources are located farther downstream in each of the shear layers, where the large-scale vortices start to interact with the impinging corners of the side branches.

When the main duct width is reduced, the increased interaction between the shear layers results in formation of a single acoustic power source region, as shown in the right plot of Fig. 12. The source is accompanied by two sinks that correspond to the regions in the shear layers where vortex development takes place. It should be noted that the source region extends across the entire opening of the coaxial side branch resonator.

4.3.2. Time-averaged acoustic power at the second hydrodynamic oscillation mode

The approximate acoustic power produced over an acoustic cycle at the second hydrodynamic oscillation mode is shown in Fig. 13.

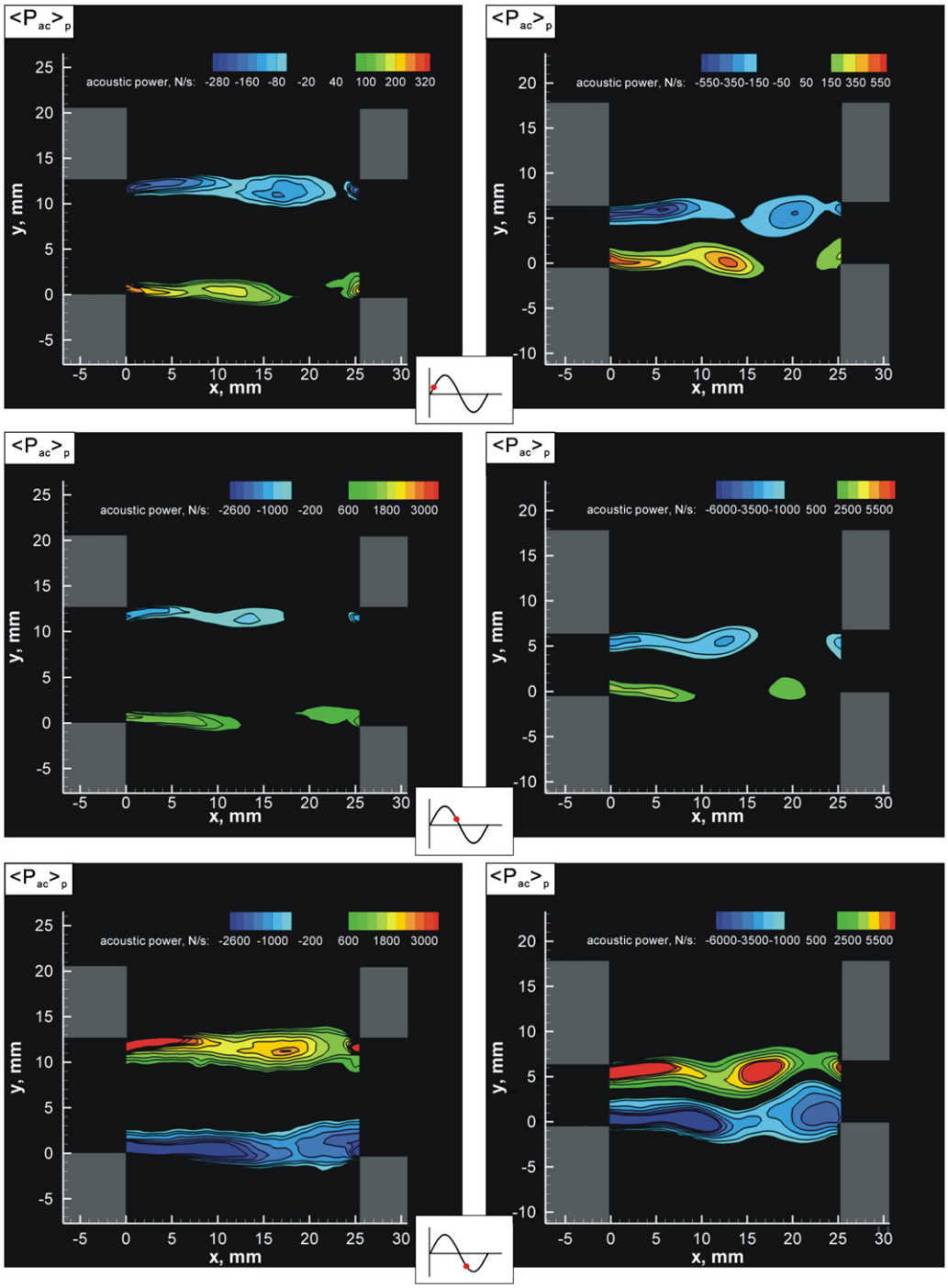

Fig. 11. Phase-averaged acoustic power corresponding to the second hydrodynamic oscillation mode. The top image illustrate the generated acoustic power at $\varphi = 10^{\circ}$. The minimum positive and negative contour levels for the case of $D = 13$ mm (left column) are $\langle\omega\rangle^{+}_{p_{\min}} = 80\,\mathrm{s}^{-1}$ and $\langle\omega\rangle^{-}_{p_{\min}} = -60\,\mathrm{s}^{-1}$, respectively. The contour increment is $\Delta\langle\omega\rangle_p = 40\,\mathrm{s}^{-1}$. The corresponding values for the case of $D = 6.5$ mm (right column) are $\langle\omega\rangle^{+}_{p_{\min}} = 150\,\mathrm{s}^{-1}$, $\langle\omega\rangle^{-}_{p_{\min}} = -150\,\mathrm{s}^{-1}$, and $\Delta\langle\omega\rangle_p = 100\,\mathrm{s}^{-1}$. In the middle images ($\varphi = 170^{\circ}$), for the case of $D = 13$ mm (left column), $\langle\omega\rangle^{+}_{p_{\min}} = 600\,\mathrm{s}^{-1}$, $\langle\omega\rangle^{-}_{p_{\min}} = -600\,\mathrm{s}^{-1}$, and $\Delta\langle\omega\rangle_p = 400\,\mathrm{s}^{-1}$. The corresponding values for the case of $D = 6.5$ mm (right column) are $\langle\omega\rangle^{+}_{p_{\min}} = 1500\,\mathrm{s}^{-1}$, $\langle\omega\rangle^{-}_{p_{\min}} = -1000\,\mathrm{s}^{-1}$, and $\Delta\langle\omega\rangle_p = 1000\,\mathrm{s}^{-1}$. In the bottom images ($\varphi = 240^{\circ}$), for the case of $D = 13$ mm (left column), $\langle\omega\rangle^{+}_{p_{\min}} = 600\,\mathrm{s}^{-1}$, $\langle\omega\rangle^{-}_{p_{\min}} = -600\,\mathrm{s}^{-1}$, and $\Delta\langle\omega\rangle_p = 400\,\mathrm{s}^{-1}$. The corresponding values for the case of $D = 6.5$ mm (right column) are $\langle\omega\rangle^{+}_{p_{\min}} = 1500\,\mathrm{s}^{-1}$, $\langle\omega\rangle^{-}_{p_{\min}} = -1000\,\mathrm{s}^{-1}$, and $\Delta\langle\omega\rangle_p = 1000\,\mathrm{s}^{-1}$.

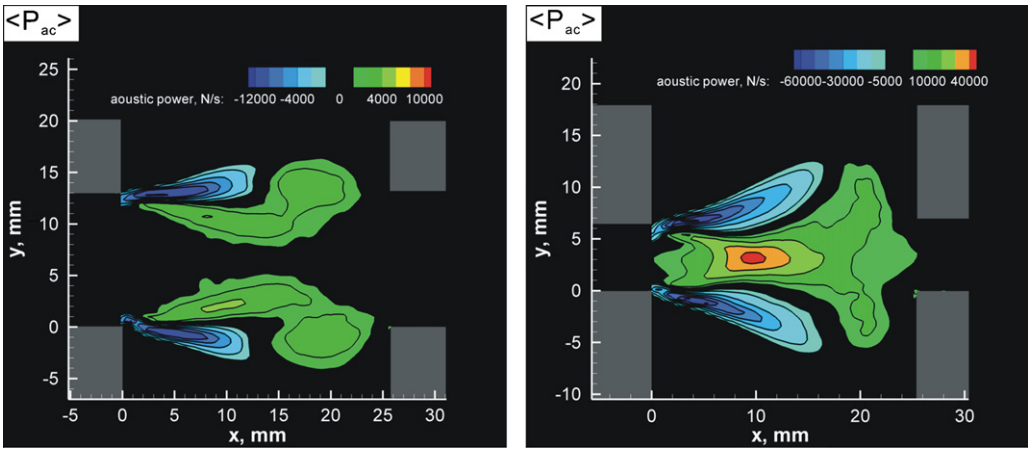

Fig. 12. Time-averaged acoustic power corresponding to the first hydrodynamic oscillation mode. The minimum positive and negative contour levels for the case of $D = 13\,\text{mm}$ (left column) are $\langle\omega\rangle^{+}_{p_{\min}} = 2000\,\text{s}^{-1}$ and $\langle\omega\rangle^{-}_{p_{\min}} = -2000\,\text{s}^{-1}$, respectively. The contour increment is $\Delta\langle\omega\rangle_p = 2000\,\text{s}^{-1}$. The corresponding values for the case of $D = 6.5\,\text{mm}$ (right column) are $\langle\omega\rangle^{+}_{p_{\min}} = 5000\,\text{s}^{-1}$, $\langle\omega\rangle^{-}_{p_{\min}} = -5000\,\text{s}^{-1}$, and $\Delta\langle\omega\rangle_p = 10\,000\,\text{s}^{-1}$.

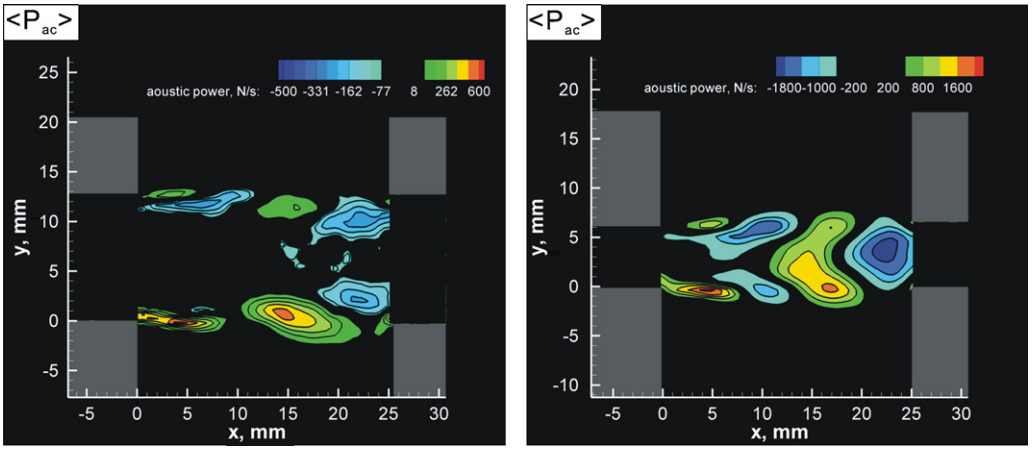

Fig. 13. Time-averaged acoustic power corresponding to the second hydrodynamic oscillation mode. The minimum positive and negative contour levels for the case of $D = 13\,\text{mm}$ (left column) are $\langle\omega\rangle^{+}_{p_{\min}} = 64\,\text{s}^{-1}$ and $\langle\omega\rangle^{-}_{p_{\min}} = -77\,\text{s}^{-1}$, respectively. The contour increment is $\Delta\langle\omega\rangle_p = 70\,\text{s}^{-1}$. The corresponding values for the case of $D = 6.5\,\text{mm}$ (right column) are $\langle\omega\rangle^{+}_{p_{\min}} = 400\,\text{s}^{-1}$, $\langle\omega\rangle^{-}_{p_{\min}} = -400\,\text{s}^{-1}$, and $\Delta\langle\omega\rangle_p = 400\,\text{s}^{-1}$.

The left-hand side plot shows the time-averaged acoustic power distribution for the case of the wide main duct. A more complex acoustic power structure is observed in comparison to that of the first hydrodynamic mode. The peak amplitude of acoustic power is significantly lower than the values observed in Fig. 12. A typical vortex traverses the mouth of the side branch in two periods of acoustic velocity oscillation. During this travel, the vortex provides two positive and two negative contributions to acoustic power. Since there is no significant interaction between the upper and lower shear layers, four discrete pairs of sink and source regions exist over the junction area. It should be noted that in the case of the second hydrodynamic oscillation mode, the dominant acoustic source region corresponds to deceleration of the large-scale vortical structures prior to their actual impingement on the downstream corner of the cavity. The peak positive values of acoustic power are observed at the downstream distance of $x = 15\,\text{mm}$ from the upstream cavity corner.

The spatial distribution of the generated acoustic power is substantially different in the case of the narrow main duct (shown in the plot on the right). While the interaction between the two shear layers is still limited immediately after the separation, two discrete source–sink pairs exist in the vicinity of the upstream corner of the junction. The two source regions with peak amplitudes of 1800 N/s are located at $x = 4\,\text{mm}$. Farther downstream, where the vortices in the upper

and lower shear layers interact with each other, a large single source region is present. This source region exhibits high levels of generated acoustic power due to increased circulation of the large-scale vortices. Prior to impingement on the downstream side branch corner, the two interacting shear layers produce a single large-scale sink region that is located at $x = 22\,\text{mm}$.

5. Conclusions

Global quantitative images of acoustically-coupled flows through coaxial side branch resonators were obtained using DPIV. A combination of the DPIV imaging with the measurements of unsteady acoustic pressure allowed characterization of the flows in terms of instantaneous, phase- and time-averaged parameters. Implementation of phase-locking techniques provides insight into the mechanisms of acoustic power generation during a typical cycle of acoustic oscillations.

The decrease of the main duct width has a pronounced effect on the acoustic power source structure due to increased interaction between the unsteady shear layers that form across the side branches. As the main duct width decreases, the patterns of the generated acoustic power corresponding to various modes of shear layer oscillation undergo a substantial change.

Acknowledgements

The authors would like to thank Dr Nedjib Djilali of the University of Victoria for providing instrumentation for this study. The authors gratefully acknowledge financial support of Natural Sciences and Engineering Research Council of Canada (NSERC) under a Discovery Grant.

References

Bruggeman, J.C., Hirschberg, A., Van Dongen, M.E.H., Wijnands, A.P.J., Gorter, J., 1989. Flow induced pulsations in gas transport systems: analysis of the influence of closed side branches. ASME Journal of Fluids Engineering 111, 484–491.

Bruggeman, J.C., Hirschberg, A., Van Dongen, M.E.H., Wijnands, A.P.J., Gorter, J., 1991. Self-sustained aero-acoustic pulsations in gas transport systems: experimental study of the influence of closed side branches. Journal of Sound and Vibration 150, 371–393.

Dequand, S., Hulshoff, S.J., Hirschberg, A., 2003a. Self-sustained oscillations in a closed side branch system. Journal of Sound and Vibration 265, 359–386.

Dequand, S., Willems, J.F.H., Leroux, M., Vullings, R., van Weert, M., Thieulot, C., Hirschberg, A., 2003b. Simplified models of flue instruments: influence of mouth geometry on the sound source. Journal of the Acoustical Society of America 113 (3), 1724–1735.

Howe, M.S., 1975. Contributions to the theory of aerodynamic sound, with applications to excess jet noise and the theory of the flute. Journal of Fluid Mechanics 71, 625–673.

Kriesels, P.C., Peters, M.C.A.M., Hirschberg, A., Wijnands, A.P.J., Iafrati, A., Riccardi, G., Piva, R., Bruggeman, J.C., 1995. High-amplitude vortex-induced pulsations in a gas transport system. Journal of Sound and Vibration 184, 343–368.

Nelson, P.A., Halliwell, N.A., Doak, P.E., 1981. Fluid dynamics of a flow excited resonance. Part I: Experiment. Journal of Sound and Vibration 78, 15–38.

Nelson, P.A., Halliwell, N.A., Doak, P.E., 1983. Fluid dynamics of a flow excited resonance, Part II: Flow acoustic interaction. The dissipation of sound at an edge. Journal of Sound and Vibration 91, 375–402.

Oshkai, P., Yan, T., Howard, A., 2005. Investigation of Acoustically-Coupled Shear Layers Using Particle Image Velocimetry. Wessex Institute of Technology, CMEM2005, Malta.

Radavich, P.M., Selamet, A., Novak, J.M., 1999. Acoustic source location in flow-excited quarter wave resonators. Internoise 99, Fort Lauderdale, FL, USA, pp. 341–346

Rockwell, D., Naudascher, E., 1978. Review of self-sustaining oscillations of flow past cavities. ASME Journal of Fluids Engineering 100, 152–165.

Ziada, S., 1994. A flow visualization study of flow-acoustic coupling at the mouth of a resonant side-branch. Journal of Fluids and Structures 8, 391–416.

Ziada, S., Bühlmann, E.T., 1992. Self-excited resonances of two side-branches in close proximity. Journal of Fluids and Structures 6, 583–601.